CONF-9003162--1

ANL-HEP-CP--90-37

DE90 011183

INTERMITTENCY STUDY IN e^+e^- ANNIHILATIONS AT 29 GeV

K. Sugano
Argonne National Laboratory, Argonne, IL 60439

Abstract:

The intermittency and fractal behavior in e^+e^- annihilations has been studied using the HRS detector at PEP ($\sqrt{s}$ = 29 GeV). The factorial moments F_i(i = 2 ~ 5) in small rapidity intervals show stronger intermittency slopes than those for the πp, $\bar{p}p$, and AA reactions. This direct measurement confirms our previous data derived from the k-values in the negative binomial fits to the multiplicity distributions in various central rapidity windows. The fractal moments G_q have been measured for the first time in e^+e^- annihilations. The Legendre transform $f(\alpha)$ derived from the fractal moments show a self-similar behavior which is consistent with the jet cascading mechanism.

An invited talk given at the Santa Fe Workshop on Intermittency in High Energy Collisions, Santa Fe, NM (March 18-21, 1990).

1. Introduction

The idea of intermittency for the multiparticle production in the high energy collisions[1] has recently generated a considerable enthusiasm in trying to understand the underlying physics of multiparticle productions at high energies. The intermittency is defined here as a power-law dependence of factorial moments F_i on the width of rapidity interval δ such that

$$F_i = \delta^{-a_i} ,$$

where the mathematical definitions of F_i and δ will be given later on. The word "intermittency" originally came from the field of fluid-dynamics physics. In an isotropic turbulent fluid of a high Reynolds number, an intermittent structure appears as tube-like regions of a high vorticity isosurface.[2] Besides the interesting developments in the physics of turbulence and chaos, it is the notion of phase transition in quark-gluon plasma[3] that motivated the application of intermittency to the multiparticle production in high energy physics. While it is still not clear whether such phase transition exists or not, there have been data in cosmic ray physics which suggest a large concentration of particles in narrow rapidity regions at very high energies.[4] The factorial moments are suited to study the fluctuations of particles event-by-event which, averaged over many events, could be smoothed away. Since there are scaling properties of statistical system in critical phenomena, the moments are also expected to show an intermittency in case of a phase transition.[5] Therefore, the normalized factorial moments in the small rapidity intervals have recently been measured in various types of collisions.[6] So far, the intermittency is strongest in e^+e^- annihilations with a hierarchy of $a_i(e^+e^-) > a_i(\text{hadron-hadron}) > a_i(\text{nucleus-nucleus})$.

The interpretation of the origin of intermittency seen in some data is not yet straight forward. Not only does the phase transition lead to a signal of intermittency, but also other mechanisms such as self-similar interactions can show an intermittency behavior. The concept of self-similarity is closely related to a fractal theory[7] and is a natural result of cascading mechanism in

the hadronization of quarks and gluons. Therefore, the analysis techniques developed in the field of fractals are also useful tools to study the underlying physics of multiparticle production. At this stage, it is necessary to approach the intermittency from various angles. More data as well as closely interplay between theory and experiment are also needed.

In the following sections, I will present data in e^+e^- annihilations and discuss their implications. I apologize in advance to all authors whose work I have omitted to mention through my negligence, ignorance, or misplaced brevity.

2. Detector and Event Selections

2.1 Detector

In this talk we report an intermittency study of the charged particle multiplicity in e^+e^- annihilations, using a high statistics data sample corresponding to a total integrated luminosity of 300 pb^{-1} obtained with the High Resolution Spectrometer (HRS) at PEP. The HRS detector, as shown in Fig. 1, was a solenoidal spectrometer that measured charged particles and electromagnetic energy over 90% of the solid angle.[8] The tracking system consisted of a vertex chamber, a central drift chamber, and an outer drift chamber. The central drift chamber had 15 cylindrical layers of drift cells. Eight of the layers had stereo wires (±60 mrad) in order to measure the z position. The momentum of a 14.5 GeV/c charged particle in the 1.62 T magnetic field was measured with a resolution of about 3%. A 40-module barrel shower counter system provided electromagnetic calorimetry over 62% of the solid angle with energy resolution below 10 GeV of $\sigma_E/E \simeq 0.16/\sqrt{E}$ (E in GeV). The beam pipe and the inner wall of the central drift chamber were made of beryllium so as to minimize photon conversions; the total material between the interaction point and the central drift chamber was less than 0.02 radiation lengths.

2.2 Event Selections

To ensure good tracking efficiency, the thrust axis of the event was selected to be within 60° of the equatorial plane of the detector, and all acceptable tracks were required to have an angle with respect to the e^+e^- beam direction (θ) of more than 24° and to register in more than one-half of the drift chamber layers traversed. Isolated tracks were reconstructed with > 99% efficiency, but for a typical annihilation event, with several close tracks, the reconstruction efficiency was lower. For $\theta > 30°$ and $p > 200$ MeV/c, the track reconstruction efficiency was 80% or better and varies slowly with dip angle; for the higher momenta, $p > 2$ GeV/c, this increased to 90%. In addition, ~ 7% of the found tracks were not valid. Low momentum tracks were not well reconstructed for any dip angle because of the high magnetic field of the spectrometer; a track with $p < 240$ MeV/c spiraled within the central drift chamber.

The events were selected with the number of acceptable charged tracks between 5 and 40. Each track had to pass within 3 cm in (x,y) radius and 15 cm in z from the interaction point. In addition, the scalar sum of the charged momenta, plus the energy registered in the barrel shower counter system, was required to be greater than 12 GeV, with at least 1 GeV in the shower counter and more than 7.5 GeV/c in charged particle. The invariant mass of three-prong jets in six-prong events was required to be greater than the τ lepton mass. These cuts, which effectively removed beam-gas interactions, examples of lepton-pair production, two-photon events, and cosmic rays, produced a data sample of about 100k events. The events passing these cuts were mixtures of the two-jet and three-jet topologies. The low sphericity region ($0 < S < 0.25$) was dominated by the two-jet events, and contained 82% of the data sample; the higher sphericity region ($0.25 < S < 1$) was strongly enriched in three-jet events. A picture of a two-jet event is shown in Fig. 2 in the kinematic region with $S < 0.25$ and $A < 0.1$, where the sphericity and aplanarity were determined by the eigenvalues of the momentum tensor.

3. Factorial Moments

3.1 Rapidity Distributions

A rapidity of each charged particle is calculated by the following formula:

$$y = \frac{1}{2} \ln \frac{E + p_{\parallel}}{E - p_{\parallel}} \quad ,$$

where E is an energy of a particle assuming it to be a pion and $p_{\parallel}$ is a momentum projected onto a thrust axis of the event. The rapidity resolution is calculated to be 0.01, based on the detector resolutions of 2 mrad for a polar angle resolution, 0.5 mrad for an azimuthal angle resolution, and 0.7% for a momentum resolution for $p < 5$ GeV/c. However, since there is an ambiguity in determining the true jet axis which is the initial quark direction, a realistic rapidity resolution is estimated to be about 0.1.

The rapidity distribution after detector corrections for the inclusive data sample is shown in Fig. 3, where only the absolute values of y are considered. The uncorrected distribution is shown in Fig. 4 for the range of $y = -5$ and $y = +5$. The narrow valley near $y = 0$ is due to the definition of a jet axis. The jet axis is determined by the thrust axis of all charged particles including a missing momentum vector which balances the total momentum vector. The broad valley between $y = -1.5$ and $y = +1.5$ is mainly because of the low tracking efficiency of slow particles and tracks near the beam line. The slight asymmetry between positive and negative rapidities is due to the direction of the jet axis. In the following analysis, we use uncorrected variables.

3.2 Azimuthal Angle Distribution

An azimuthal angle (ϕ) of each charged track with respect to the beam axis is calculated. This should be distinguished from the azimuthal angle with respect to the jet axis. Although ϕ's in each event are clustered in narrow phase space regions due to the jet structure of events, the averaged distribution over many events is expected to be flat as shown in Fig. 5. This

variable is well suited for the technical study of intermittency and fractal theories because it is invariant under Lorentz transformations, its distribution is quite flat thus eliminating the need for detector corrections, and it is easy to visualize the intermittent structure in terms of narrowly collimated jets.

3.3 Normalized Factorial Moments

A rapidity interval of total length Y_o is divided into M equal intervals of length $\delta y = Y_o/M$. A normalized i^{th} factorial moment is defined as follows:

$$F_i = \left\langle \frac{1}{M} \sum_{m=1}^{M} \frac{k_m (k_m - 1) \ldots (k_m - i + 1)}{N(N - 1) \ldots (N - i + 1)} M^i \right\rangle ,$$

where k_m is the number of particles in the m^{th} bin of length δy with $1 \le m \le M$, N is the total number of particles in the rapidity interval of Y_o, thus $N = k_1 + k_2 + \ldots + k_M$, and $\langle\ \rangle$ means the average is taken over all events.

The rapidity range is selected to be between $y = -2$ and $y = +2$ and the maximum number of divisions is 40, which corresponds to the minimum bin size of $\delta y = 0.1$. Resulting factorial moments F_i ($i = 2 \sim 5$) are shown in Fig. 6, where the abscissa is $-\ln\delta y$ and the ordinate is $\ln F_i$. The error bars are statistical only. The slopes (a_i) of $\ln F_i$ in the small δy region (typically $-\ln\delta y \gtrsim 0.5$) are listed in Table 1. These results are consistent with the recent TASSO data[9] and the slopes in e^+e^- annihilations are larger than those in hadron-hadron (hh) and nucleus-nucleus (AA) collisions. Figure 7 and 8 show similar plots for the full rapidity range of $Y_o = 10$ and for the 2-jet sample, respectively.

An azimuthal angle interval of total length ϕ_o is also studied in a similar way. The factorial moments with $\phi_o = 2\pi$ are shown in Fig. 9 where the abscissa is the number of divisions and the ordinate is the averaged factorial moments both in log scales. There are definite linear relationships for all F_i in log-log plot in the region of $M \gtrsim 10$ reflecting the intermittent behavior of jet events. Figure 10 is for the 2-jet sample and the slopes are larger than those for the inclusive sample. This is explained by the 2-jet structure of events which is narrowly collimated and back-to-back.

3.4 Factorial Moments at Fixed Rapidity Values

Indirect values of F_2 and F_3 in e^+e^- annihilations have been calculated[10] using the k-values from the negative binomial fit to the multiplicity distributions in various rapidity windows.[11] In order to compare these values with the direct measurement, we use a slightly different normalization of factorial moments:

$$\langle F_i \rangle = \frac{\langle n(n-1) \ldots (n-i+1) \rangle}{\langle n \rangle^i} ,$$

where n is the number of charged particles in a bin of size δy at a fixed rapidity value and $\langle\ \rangle$ denotes an average over all events.

The factorial moments at y = 0 for the inclusive sample are plotted in Fig. 11, together with those from k's in negative binomial fits. The agreement between the calculated values and the direct measurements is generally good, although the statistical errors of the direct measurements in the small δy region are large due to the lack of "horizontal" averaging. The factorial moments at different y's (y center = 0.5 and 1) are shown in Fig. 12 and Fig. 13. It is intriguing that the moments differ somewhat according to the positions in rapidity space. Some theories predict different moments at different rapidity points. However, the statistical errors are large and it could be due to the nonuniformity of the rapidity distribution. A similar trend is observed in the data for the 2-jet sample as shown in Figs. 14, 15, and 16.

4. Fractal Moments

4.1 Definition of Multifractal Moments

A rapidity range of Y_0 is divided into M_0 bins of width $\delta = Y_0/M_0$ and let k_i be the number of particles in the i^{th} bin. Since there may be bins that have no particles, we define M to be the number of non-empty bins, which constitute a fractal set.

A multifractal moment is defined as follows[12]:

$$G_q = \sum_{j=1}^{M} p_j^q \quad ,$$

where $p_j = k_j/n$ with $n = k_1 + k_2 + \ldots + k_M$, q is a real number, and the summation is carried over non-empty bins only. If the particle production process exhibits self-similar behavior, the moments show a power law relation of $G_q \propto \delta^{\tau(q)}$. This relation does not necessarily occur in the limit of $\delta \to 0$. Once $\tau(q)$ is determined from G_q, we can apply the theory of multifractals to calculate $f(\alpha)$ by Legendre transform:

$$\alpha_q = \frac{d\tau(q)}{dq}$$

$$f(\alpha) = q\alpha_q - \tau(q) \quad .$$

4.2 Multifractal Moments in ϕ Space

We start with a study of multifractal moments in azimuthal angles with respect to the beam axis because it is easier to interpret the results in terms of multijet structure. The multifractal moments with the full ϕ range ($\phi_o = 2\pi$) are shown in Fig. 17, where the abscissa is the number of divisions ($M_o = 2^\nu$) and the ordinate is an average of $\ell n G_q$ over all events. The moments with positive q-values show a linearity over a wide range in ν, but those with negative q-values tend to saturate as ν becomes larger. In calculating the slope with the following formula

$$\tau(q) = -\frac{1}{\ell n 2} \frac{d\ell n G_q}{d\nu}$$

we used the first two points in ν, i.e., $M_o = 2$ and 3. The $\tau(q)$ averaged over all events is plotted as a function of q in Fig. 18, and the Legendre transform $f(\alpha)$ is shown in Fig. 19. The left-hand side of the $f(\alpha)$ curve ($q > 0$) is sensitive to the peaks in the ϕ distribution and the right-hand side ($q < 0$) to the valleys. The broad width of the curve means that the particles are tightly bunched together in the ϕ space and there is wide space between the bunches for almost every event as expected with the jet structure of

events. This can be compared to the narrow delta function at $\alpha = 1$ which is the result of a constant distribution for arbitrary small δ.

The G_q, $\tau(q)$, and $f(\alpha)$ for the 2-jet sample are shown in Figs. 20, 21, and 22, respectively. The $f(\alpha)$ is even wider reflecting the back-to-back narrow jets. If the ϕ_o is restricted in a smaller range ($\phi_o = \pi$), the multifractal moments become smaller as shown in Fig. 23 and the $\tau(q)$ gets flatter as shown in Fig. 24. The $f(\alpha)$ shown in Fig. 25 shifts to the smaller α and the width becomes narrower. These tendencies can be understood in terms of the size of phase space. The smaller the ϕ_o range is, the finer is the structure in the region investigated for the given number of divisions. Figures 26, 27, and 28 are respectively the G_q, $\tau(q)$, and $f(\alpha)$ for the Lund Monte Carlo events (JETSET 5.3)[13] after detector simulation. The left-hand side of $f(\alpha)$ in Fig. 28 agrees well with the data in Fig. 19, but there are some discrepancies with the right-hand side. This can be attributed to the lack of fine tuning of the Lund model in the region between jets where coherence effects show up.

4.3 Multifractal Moments in y Space

The multifractal moment in the rapidity space is a powerful tool to study the self-similarity in the hadronization mechanism in jets. If quarks and gluons become jets of particles through a cascading process, then the particles inside a jet should show a self-similar behavior due to its fractal structure of the tree-branching. Furthermore, the $f(\alpha)$ is sensitive to the models of various parton branchings. The multifractal moments for the inclusive data sample with the rapidity range between $y = -2$ and $y = +2$ are shown in Fig. 29, where the abscissa is $-\ell n\delta y$ and the ordinate is an average of ℓnG_q over all events. All the moments show a saturating behavior in the large $-\ell n\delta y$ region. The slopes are calculated using the first two points ($-\ell n\delta y = -0.693$ and -0.288) with a formula;

$$\tau(q) = \Delta \langle \ell nG_q \rangle / \Delta \ell n\delta y \quad .$$

The $\tau(q)$ is shown in Fig. 30 as a function of q. The curve flattens for the

positive q-values, which is a feature of a gluon model compared to a ϕ^3 model.[14] The Legendre transform $f(\alpha)$ is plotted in Fig. 31. Compared to the $f(\alpha)$ in the ϕ space in Fig. 19, the curve in the y space is narrower and the peak position is shifted to the smaller α-values. The tangential position ($q = 1$) remains almost the same. The generalized dimensions $D_q = \tau(q)/(q - 1)$ are derived and listed in Table 1. The end points of the curve ($q = \pm\infty$) seem to be all positive, which can be interpreted as "no phase transition" in the α-model.[15]

A different averaging technique for G_q has also been tried. The G_q's, instead of $\ell n G_q$'s, were averaged arithmetically over all events and then a logarithm was taken. The difference is that the previous $< \ell n\, G_q >$ is a logarithm of a geometrical average of G_q while this $\ell n < G_q >$ is a logarithm of an arithmetic average of G_q. The $\ell n< G_q >$ moments are shown in Fig. 32. As expected, the arithmetic average is always larger than the geometric average. The tendency of saturation is similar. The $\tau(q)$ plotted in Fig. 33 show a stronger flattening for $q > 1$. Consequently, the $f(\alpha)$ is wider as shown in Fig. 34.

Figures 35, 36, and 37 are respectively the multifractal moments ($< \ell n\, G_q >$), $\tau(\alpha)$, and $f(\alpha)$ for the 2-jet sample with a rapidity window of $Y_o = 4$. Different rapidity windows have been tried for the inclusive data sample. The multifractal moments with $Y_o = 2$, shown in Fig. 38, become smaller than those with $Y_o = 4$ and as a result, the $\tau(q)$ shown in Fig. 39 is flatter. The $f(\alpha)$ curve, shown in Fig. 40, shifts to the left and the width is much narrower. This can be explained in a similar manner as the previous case of $\phi_o = \pi$. The multifractal moments with $Y_o = 10$ are shown in Fig. 41, where some structures appear near $-\ell n\delta y = -1$. This is due to the rapidity distribution which has a steep fall-off beyond $|y| > 2$. The $\tau(q)$ is calculated using the first two points of the moments as before, although it is no longer the steepest slope for $q > 0$. The resulting $\tau(q)$ and $f(\alpha)$ are shown in Fig. 42 and Fig. 43, respectively. The general feature of the unusually wide $f(\alpha)$ curve can be explained by the rapidity distribution. The edges of the rapidity distribution contribute to the moments in both positive and negative q-values, thus widening both sides of the $f(\alpha)$ curve. Therefore, a caution should be

exercised when a strongly nonuniform portion of an averaged distribution is selected for an initial window in studying its multifractal structure.

Finally, the Lund Monte Carlo events, after detector simulation, are compared to the data. The multifractal moments with $Y_o = 4$ for the inclusive sample are shown in Fig. 44. The agreement with the data shown in Fig. 29 is almost perfect. A slight difference can be seen in the $\tau(\alpha)$ plot shown in Fig. 46. The $f(\alpha)$ is the best among the three plots to see the differences as well as the general features. The left-hand side of $f(\alpha)$ is in almost perfect agreement with the data shown in Fig. 31. This means that the Lund Monte Carlo is already well-tuned even in terms of fluctuation of particle multiplicities. The right-hand side of $f(\alpha)$ is slightly wider than the data, indicating again that the tuning of the model is not perfect in the region between jets where coherence effects are important.

5. Summary and Conclusions

The intermittency and fractal behavior in e^+e^- annihilations at 29 GeV has been studied. The normalized factorial moments in the rapidity space show a power law relation in the region of small rapidity intervals which is called intermittency phenomena. The slopes of the i^{th} factorial moments F_i in the ℓnF_i - $\ell n\delta y$ plane are measured with the same normalization formula as the TASSO group used. The results are consistent with each other. The slope a_i increases as the index i becomes larger. Comparing the data of a_5 for various types of collisions such as e^+e^-, π^+p, $\bar{p}p$, and SS, there is a hierarchy of $a_i(e^+e^-) > a_i(hh) > a_i(AA)$, where hh is a hadron-hadron collision and AA a nucleus-nucleus collision. The normalized factorial moments in the azimuthal angle space with respect to the beam axis show even stronger behavior of intermittency. This is explained by the jet structure of events.

The factorial moments at fixed rapidity positions have been measured with a slightly different normalization formula. They are consistent with the F_2 and F_3 calculated from the k-values in the negative binomial fits to the multiplicity distributions in various rapidity windows. Although the statistics is limited due to a lack of horizontal averaging, there is a hint

that F_i changes according to the position in the rapidity distribution. The effects of various detector corrections are under investigation.

The multifractal moments G_q have been measured for the first time. The slope $\tau(q)$ and the Legendre transform $f(\alpha)$ are calculated. This new approach reveals the fractal structure of the multiparticle production. If quarks and gluons become jets of particles through a cascading process, the particles inside a jet should show a self-similar behavior which leads to a fractal structure. The results are consistent with this interpretation of jet formations, although there are still other models that can explain the data.

The azimuthal angle with respect to the beam axis is a convenient measure for developing various analysis techniques of models. Since each e^+e^- event has a distinct structure of clustered multi-jets, the general feature of moments can be interpreted visually in terms of spatial distributions of particles in jets. The flatness of the azimuthal angle distribution averaged over all events eliminates the need for detector corrections such as acceptance and tracking efficiency.

The multifractal moments in the rapidity space are sensitive to the underlying physics of the hadronization of quarks and gluons into jets of particles. The $f(\alpha)$ in the rapidity range $y = -2$ and $y = +2$ show a peak at $\alpha = 0.81 \pm 0.02$ with a fractal dimension of $D_0 = 0.75 \pm 0.04$. The width of the curve is narrower than the prediction by a gluon model at very high energies but definitely wider than that by a ϕ^3 model. Other higher generalized dimensions have also been derived and give further information on the dynamics of particle production mechanisms. The data with smaller rapidity range ($Y_0 = 2$) and full rapidity range ($Y_0 = 10$) are consistent with the expectations based on the rapidity distribution. The Lund Monte Carlo events after detector simulation agree very well with the data in the $q > 0$ range, but differ slightly in the $q \leq 0$ range. This indicates that the fluctuation of particles inside a jet is well tuned in the Lund model (JETSET 5.3) but not yet in the valley regions between jets where coherence effects show up.

Acknowledgments

I would like to thank Rudy Hwa for bringing my attention to the recent developments of intermittency and fractal studies in high energy particle productions. I am grateful of his frequent correspondence and encouragement. I would also like to thank the members of the organizing committee of this lively workshop. I am indebted to the stimulating and enlightening conversations with Charles Chiu, Gösta Gustafson, Rudy Hwa, Jun Iwai, W. Kittel, Wolfgang Ochs, Robi Peschanski, Ina Sarcevic, Helmut Satz, Dave Seibert, and C. C. Shih.

This work was supported in part by the U.S. Department of Energy, Division of High Energy Physics, under contract W-31-109-ENG-38.

References

1. A. Bialas and R. Peschanski, Nucl. Phys. B273, 703 (1986); Nucl. Phys. B308, 803 (1988).

2. A. S. Monin and A. M. Yaglom, "Statistical Fluid Mechanics", Vols. 1 and 2, MIT Press, Cambridge, MA (1971, 1975).

3. J. D. Bjorken, Phys. Rev. D27, 140 (1983).

4. F. Takagi, Phys. Rev. Lett. 53, 427 (1984); JACEE Collaboration, Phys. Lett. 138B, 304 (1984).

5. H. Satz, Nucl. Phys. B326, 613 (1989).

6. W. Kittel, in Proc. of the 24th Intl. Conf. on High Energy Physics, Munich, 1988, eds. R. Kotthaus and J. H. Kuhn (Springer-Verlag, Berlin, 1989) p. 625; W. Kittel and R. Peschanski, in Proc. of the 1989 EPS Conference, Madrid, 1989.

7. B. Mandelbrot, "The Fractal Geometry of Nature", (Freeman, New York, 1982); J. Fluid, Mech. 62, 331 (1974).

8. D. Bender et al., Phys. Rev. D31, 1 (1985).

9. W. Braunschweig et al., DESY 89-092 (1989).

10. B. Buschbeck, P. Lipa, and R. Peschanski, Phys. Lett. B215, 788 (1988).

11. M. Derrick et al., Phys. Let. 168B, 299 (1986);
K. Sugano, Intl. J. Mod. Phys. A3, 2249 (1988).

12. R. Hwa, OITS-430 (1989).

13. B. Andersson et al., Phys. Rep. 97, 32 (1983).

14. C. Chiu and R. Hwa, OITS-431 (1990)

15. R. Peschanski, Nucl. Phys. B237, 144 (1989).

Table Captions

1. The intermittency slopes (a_i) of the $-\ell n\delta y$ vs. ℓnF_i plot in the small δy region ($-\ell n\delta y \gtrsim 0.5$).

2. The generalized dimensions $D_q = \tau(q)/(q - 1)$ of fractal moments for the rapidity range between $y = -2$ and $y = +2$.

Table 1

a_i	Flat Rapidity Region $Y_o = 4$	Full Rapidity Region $Y_o = 10$
a_2	0.021 ± 0.002	0.025 ± 0.003
a_3	0.063 ± 0.009	0.073 ± 0.010
a_4	0.202 ± 0.080	0.245 ± 0.100
a_5	0.469 ± 0.250	0.623 ± 0.340

Table 2

D_q	Name	e^+e^- data for $Y_o = 4$
$D_0 = f(\alpha_o)$	fractal dimension	0.75 ± 0.04
$D_1 = \alpha_1 - f(\alpha_1)$	information dimension	0.70 ± 0.03
$D_2 = 2\alpha_2 - f(\alpha_2)$	correlation dimension	0.65 ± 0.03

Figure Captions

1. The HRS detector.

2. The 2-jet event seen from the beam line.

3. The rapidity distribution ($|y|$) of charged particles for the inclusive data sample after detector corrections such as acceptance and tracking efficiency.

4. The rapidity distribution (y) without detector corrections. The narrow valley near y = 0 is due to the definition of the jet axis. The jet axis was determined by the thrust axis of all charged particles including a missing momentum vector which balances the total momentum vector. The broad valley between y = -1.5 and y = +1.5 is mainly due to the low tracking efficiency of slow particles and tracks near the beam line.

5. The azimuthal distribution (ϕ) of charged particles for the inclusive sample. The ϕ is with respect to the beam axis.

6. The normalized factorial moments (F_i) of charged particles in the rapidity range between y = -2 and y = +2 for the inclusive sample. The definition of the factorial moments are described in the text. The abscissa is $-\ln\delta y$, where δy is a rapidity window Y_o/M (M = 1, 2, 3, ..., 40).

7. The factorial moments for the inclusive sample in the full rapidity range.

8. The factorial moments for the 2-jet sample. The cuts for the 2-jets are $S < 0.25$ and $A < 0.1$, where S is a sphericity and A is an aplanarity.

9. The normalized factorial moments of charged particles in the full

azimuthal angle range between $\phi = 0$ and $\phi = 2\pi$. The abscissa is the number of divisions of ϕ_o.

10. The factorial moments in the ϕ space for the 2-jet sample.

11. The normalized factorial moments at the rapidity center of $y = 0$ (without horizontal averaging) averaged over all events for the inclusive sample. The normalization factor is described in the text. Superimposed are the data derived from the k-values in negative binomial fits to the distributions in various rapidity windows.

12. The factorial moments at $y = 0.5$ for the inclusive sample.

13. The factorial moments at $y = 1$ for the inclusive sample.

14. The factorial moments at $y = 0$ for the 2-jet sample.

15. The factorial moments at $y = 0.5$ for the 2-jet sample.

16. The factorial moments at $y = 1$ for the 2-jet sample.

17. The fractal moments (G_q) of charged particles in the azimuthal angle range between $\phi = 0$ and $\phi = 2\pi$ for the inclusive sample. The definition of the fractal moments is described in the text. The abscissa is the number of divisions $M = 2^{\nu}$.

18. The slopes $\tau(q)$ between $M = 2$ and $M = 3$ of the fractal moments for various q-values.

19. The spectrum $f(\alpha)$ of α for the fractal moments in ϕ. $f(\alpha)$ and α are Legendre transforms described in the text.

20. The fractal moments in the ϕ space for the 2-jet sample.

21. The $\tau(q)$ for the 2-jet sample.

22. The $f(\alpha)$ for the 2-jet sample.

23. The fractal moments in the reduced range between $y = 0$ and $y = \pi$ for the inclusive sample.

24. The $\tau(q)$ for the reduced ϕ range for the inclusive sample.

25. The $f(\alpha)$ for the reduced ϕ range for the inclusive sample.

26. The fractal moments in the ϕ space for the Lund Monte Carlo events (JETSET 5.3) after detector simulation.

27. The $\tau(q)$ in the ϕ space for the Lund Monte Carlo events.

28. The $f(\alpha)$ in the ϕ space for the Lund Monte Carlo events.

29. The fractal moments of charged particles in the rapidity range between $y = -2$ and $y = +2$ for the inclusive sample.

30. The $\tau(q)$ in the y space for the inclusive sample.

31. The $f(\alpha)$ in the y space for the inclusive sample.

32. The fractal moments in the y space for the inclusive sample. The logarithm was taken after averaging the moments arithmetically.

33. The $\tau(q)$ from $\ell n\langle G_q \rangle$.

34. The $f(\alpha)$ from $\ell n\langle G_q \rangle$.

35. The fractal moments in the y space for the 2-jet sample.

36. The $\tau(q)$ in the y space for the 2-jet sample.

37. The $f(\alpha)$ in the y space for the 2-jet sample.

38. The fractal moments in the reduced rapidity range between y = -1 and y = +1 for the inclusive sample.

39. The $\tau(q)$ in the reduced y range for the inclusive sample.

40. The $f(\alpha)$ in the reduced y range for the inclusive sample.

41. The fractal moments in the full rapidity range of y = -5 and y = +5 for the inclusive sample.

42. The $\tau(q)$ in the full rapidity range for the inclusive sample.

43. The $f(\alpha)$ in the full rapidity range for the inclusive sample.

44. The fractal moments in the rapidity range between y = -2 and y = +2 for the Lund Monte Carlo events (JETSET 5.3) after detector simulation.

45. The $\tau(q)$ in the y space for the Lund Monte Carlo events.

46. The $f(\alpha)$ in the y space for the Lund Monte Carlo events.

HIGH RESOLUTION SPECTROMETER

ARGONNE-INDIANA-MICHIGAN-PURDUE-SLAC-LBL

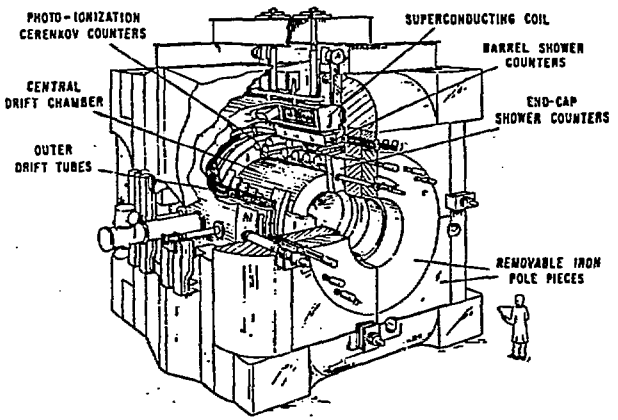

Fig. 1

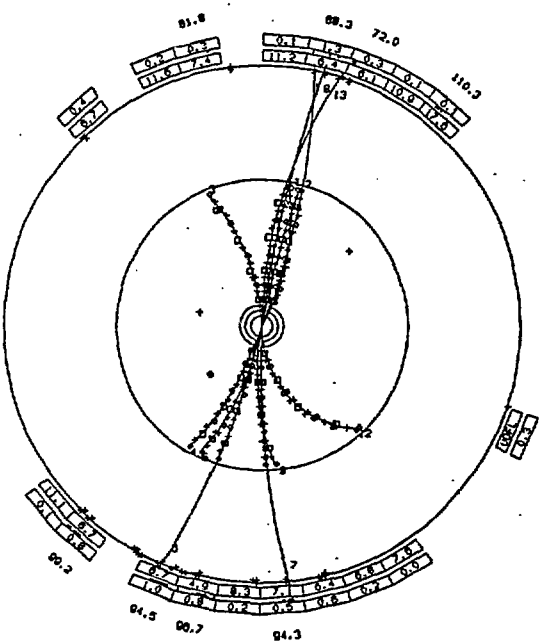

H R S RUN=4509

EVENT= 9430
DCHITS = 234
NPRNG = 14
SH SUM= 7.2 + 0.0

TRACK	MOMENTUM	THETA
1	-2.4	93.4
2	3.3	93.3
3	-0.7	77.5
4	1.1	90.9
5	0.9	99.2
6	2.5	90.9
7	-3.3	92.0
8	4.3	88.5
9	-0.9	97.9
11	-0.8	82.1
12	-0.4	88.3
13	1.7	71.2

ECODE = 52 MPRNG TOT. ENRGY

TRIG.= F1 F2 F3 S6 A2 D1 D2

Fig. 2

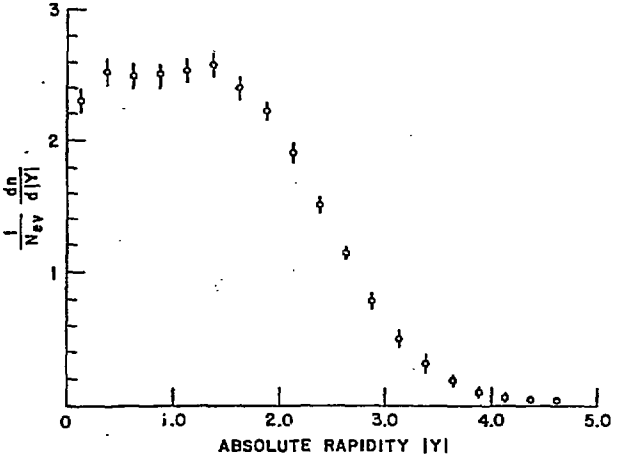

Fig. 3

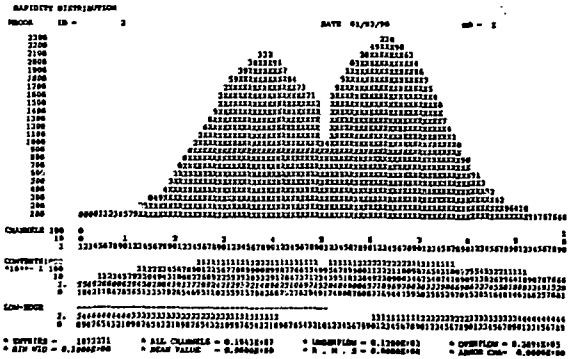

Fig. 4

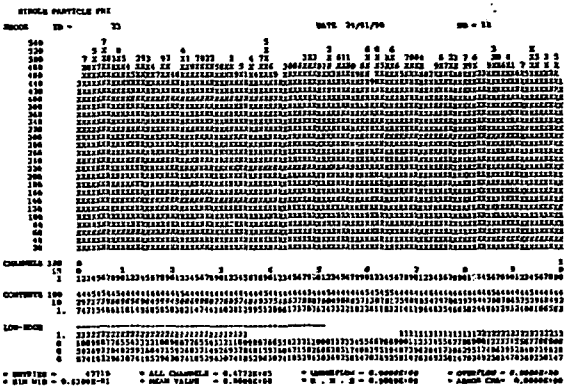

Fig. 5

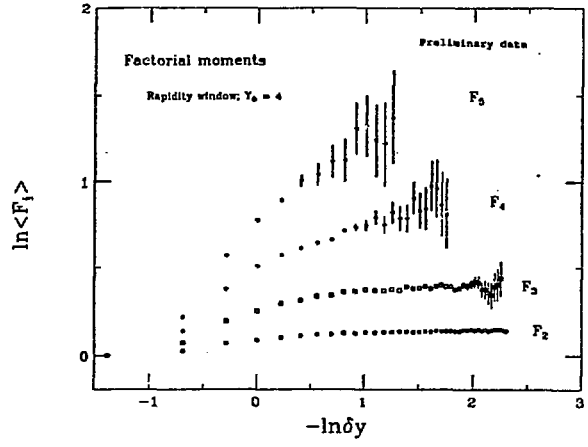

Fig. 6

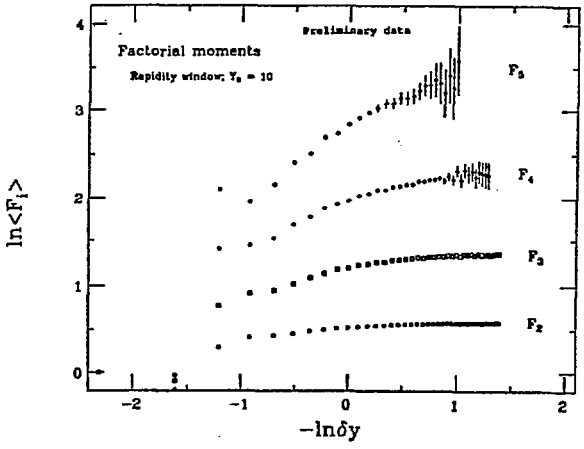

Fig. 7

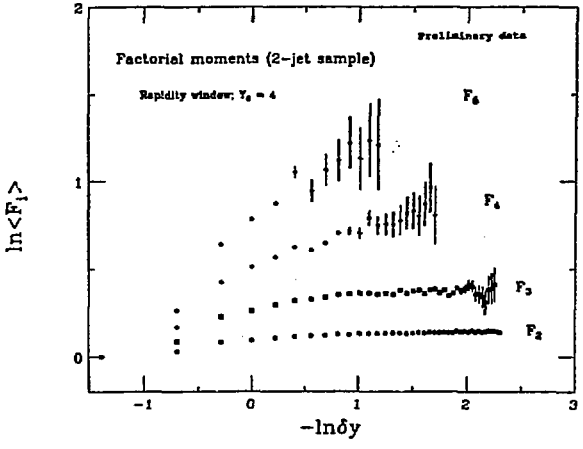

Fig. 8

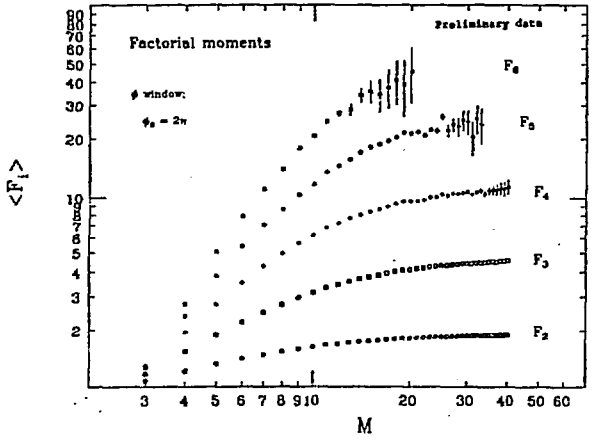
Factorial moments
Preliminary data
φ window:
$\phi_w = 2\pi$
F_6
F_5
F_4
F_3
F_2
$\langle F_i \rangle$
M

Fig. 9

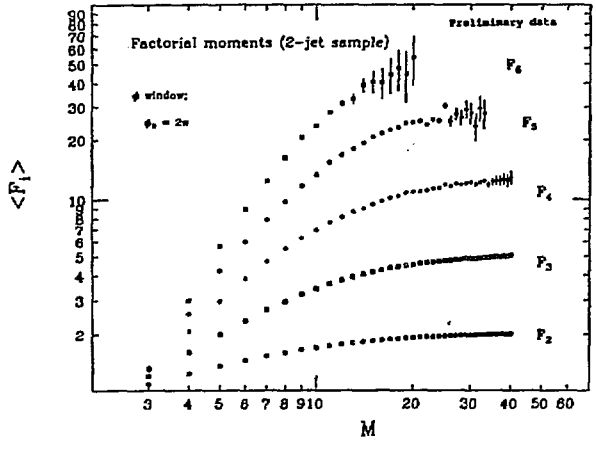
Factorial moments (2-jet sample)
Preliminary data
φ window:
$\phi_w = 2\pi$
F_6
F_5
F_4
F_3
F_2
$\langle F_i \rangle$
M

Fig. 10

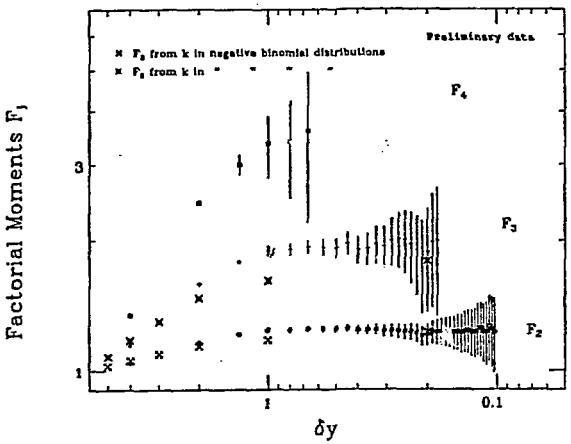

Fig. 11

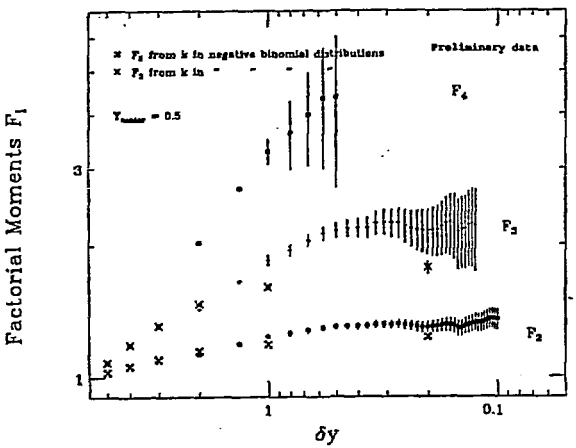

Fig. 12

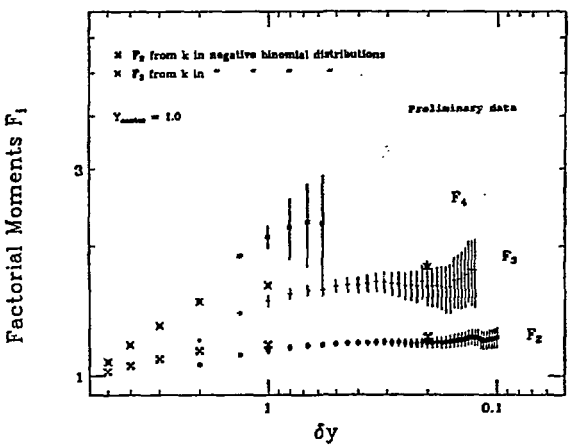

Fig. 13

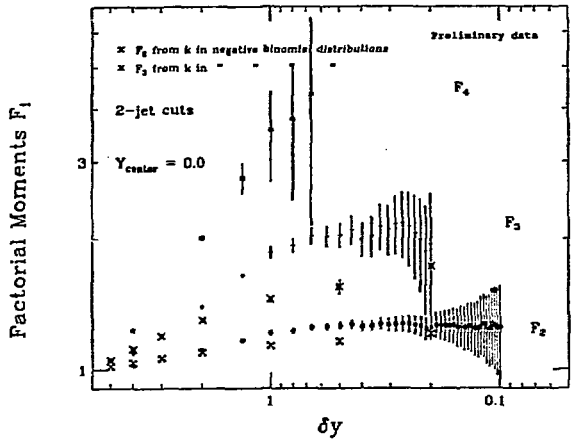

Fig. 14

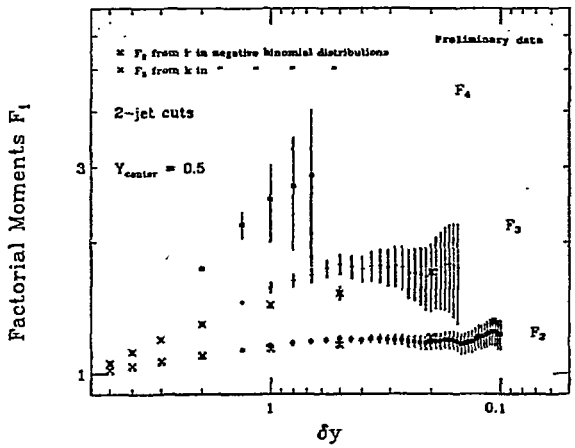

Fig. 15

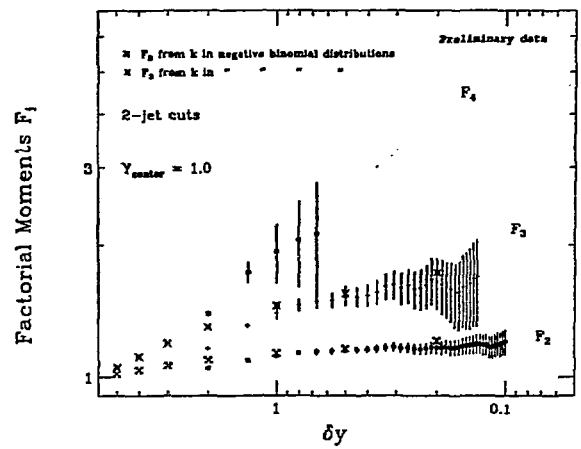

Fig. 16

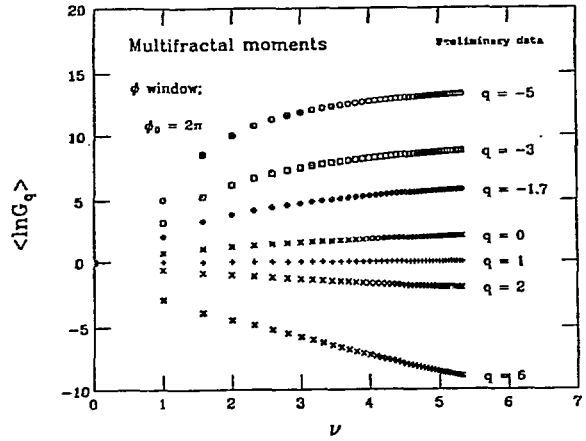

Fig. 17

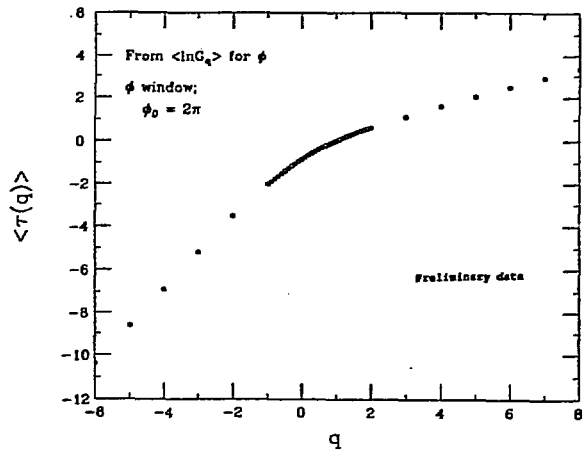

Fig. 18

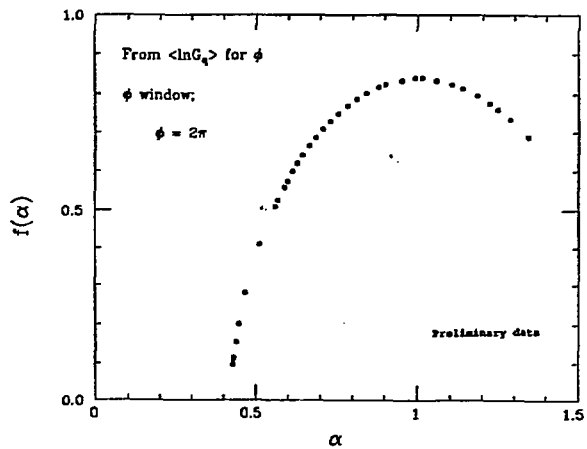

Fig. 19

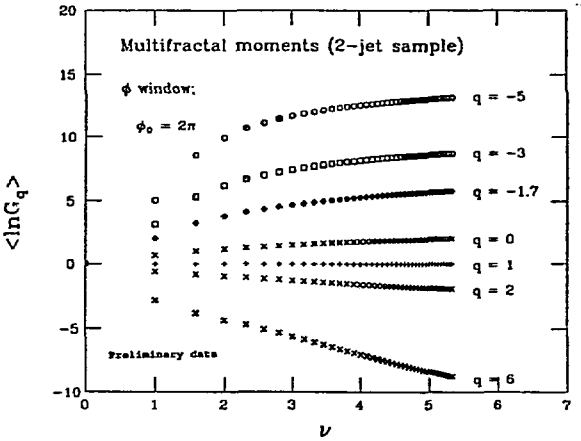

Fig. 20

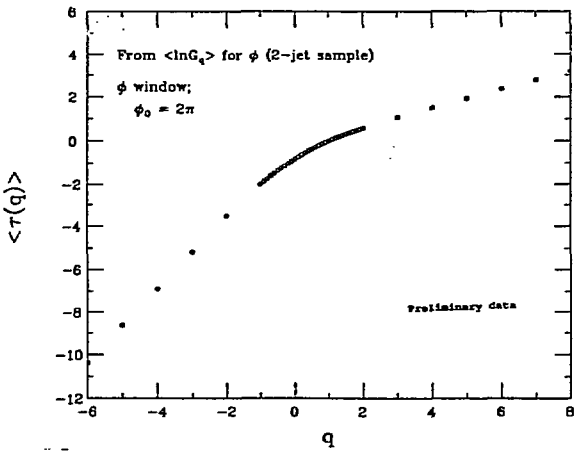

Fig. 21

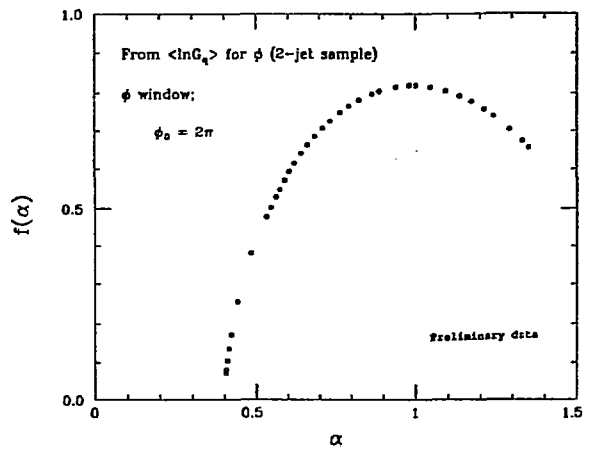

Fig. 22

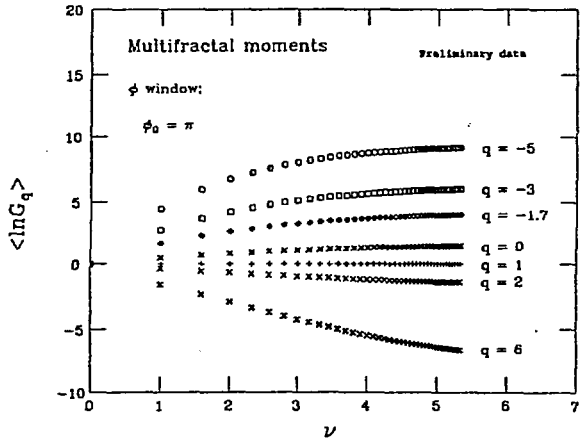

Fig. 23

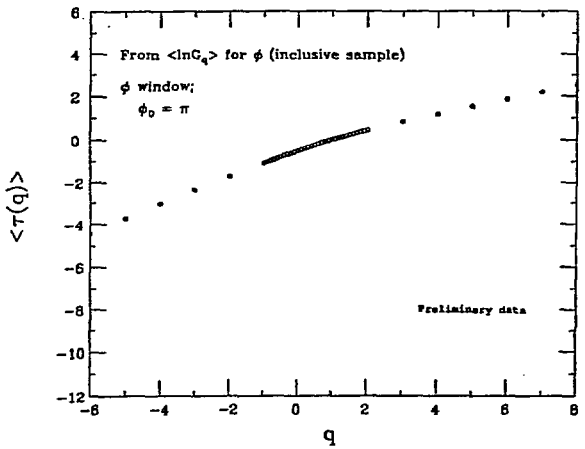

Fig. 24

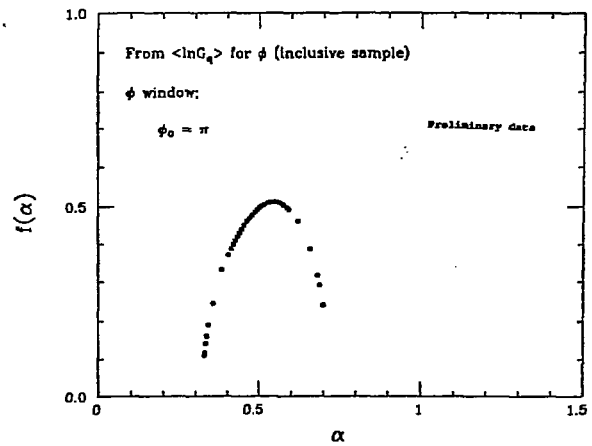

Fig. 25

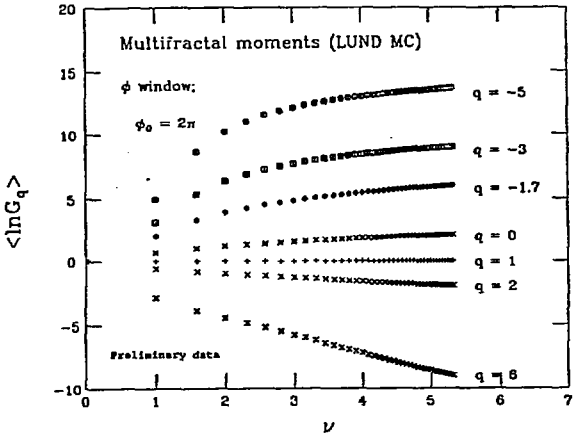

Fig. 26

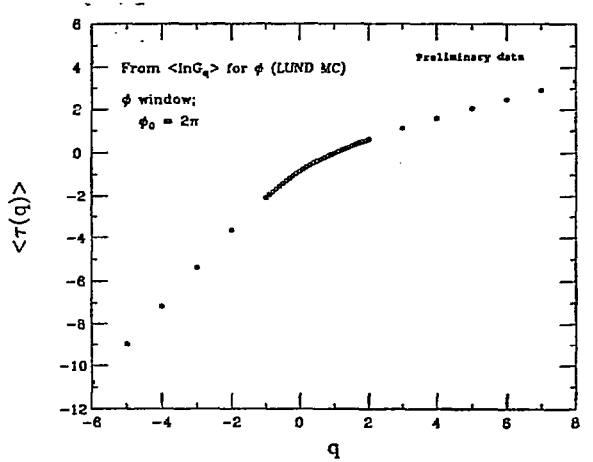

Fig. 27

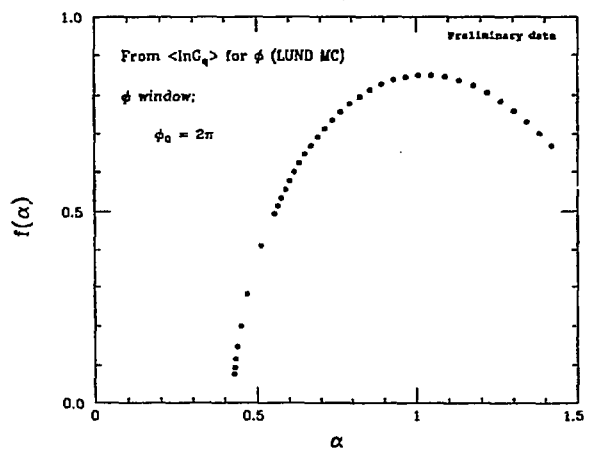

Fig. 28

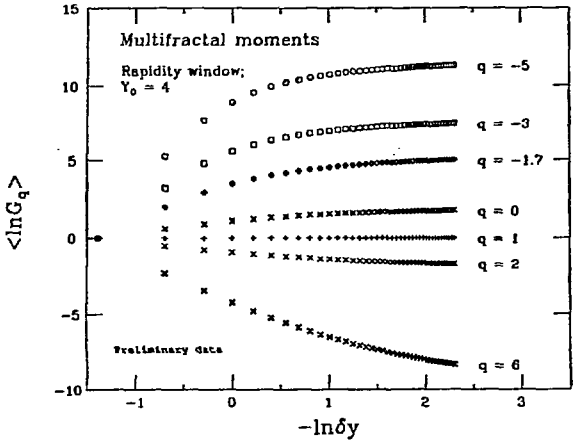

Fig. 29

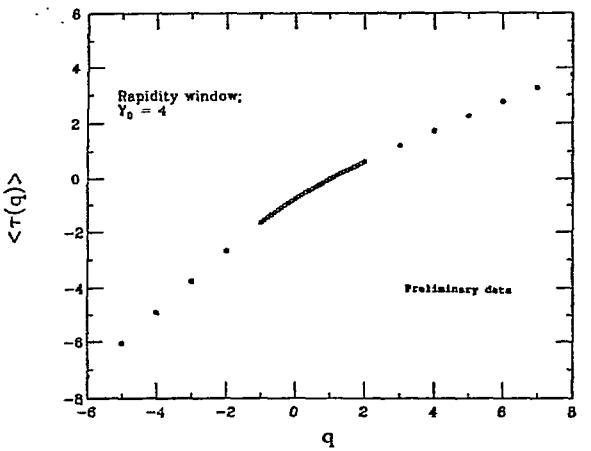

Fig. 30

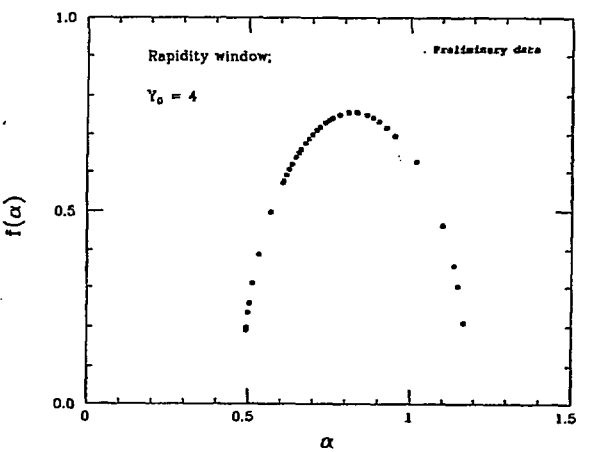

Fig. 31

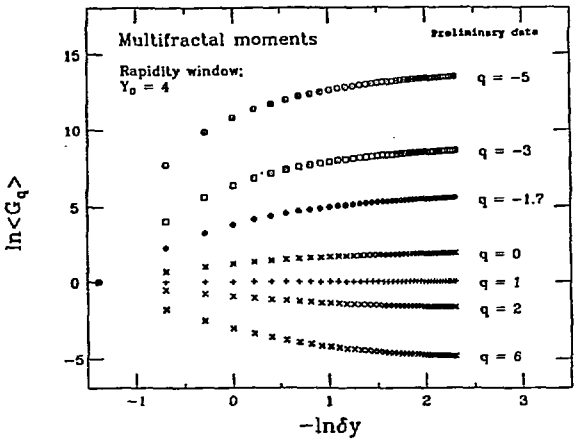

Fig. 32

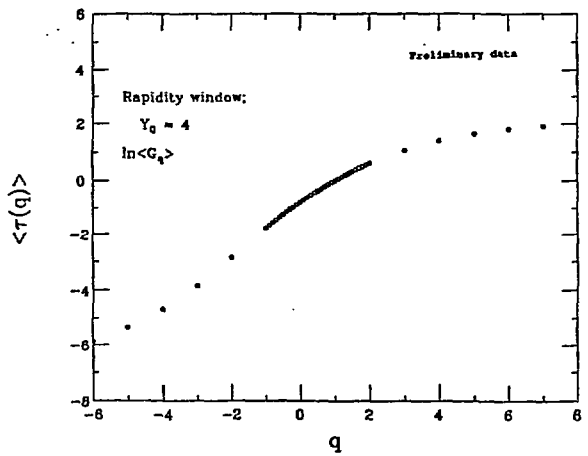

Fig. 33

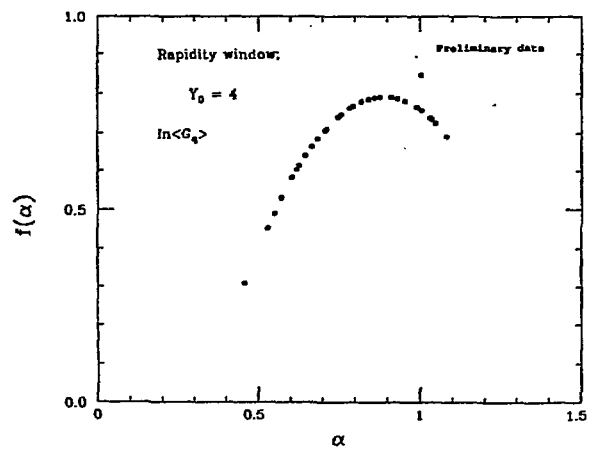

Fig. 34

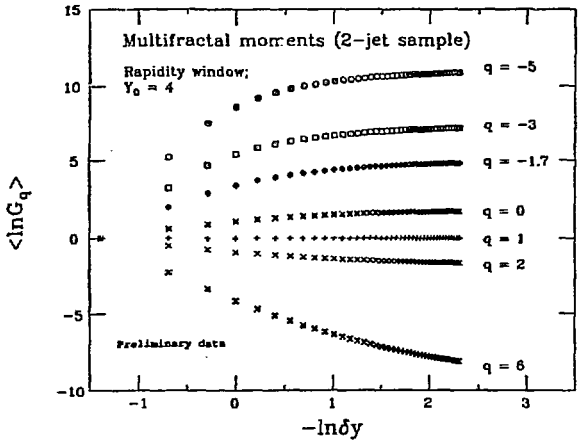

Fig. 35

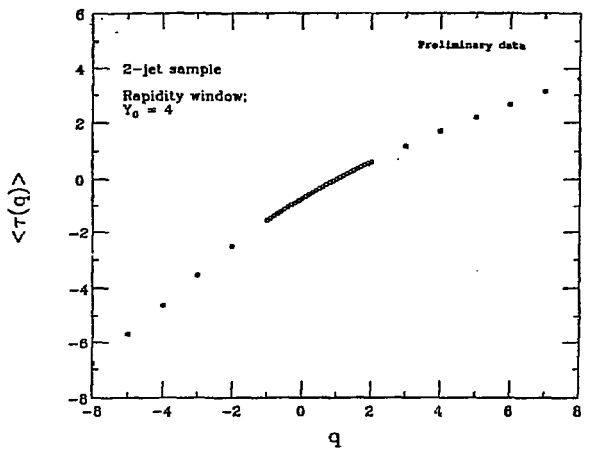

Fig. 36

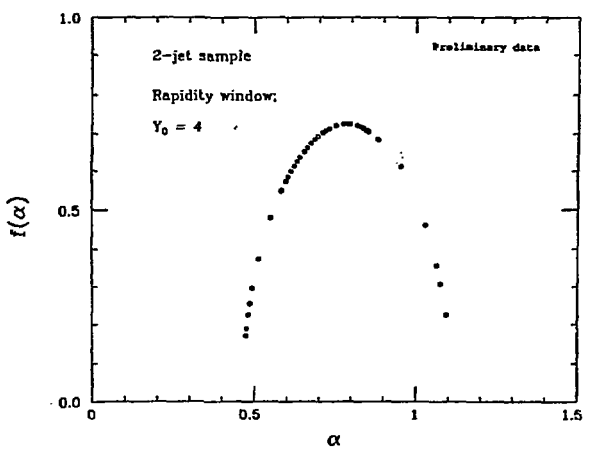

Fig. 37

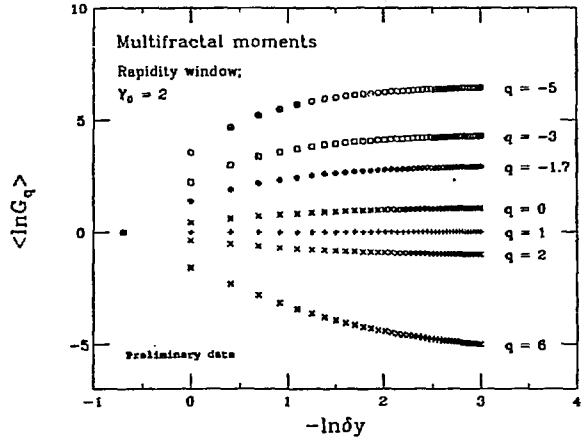

Fig. 38

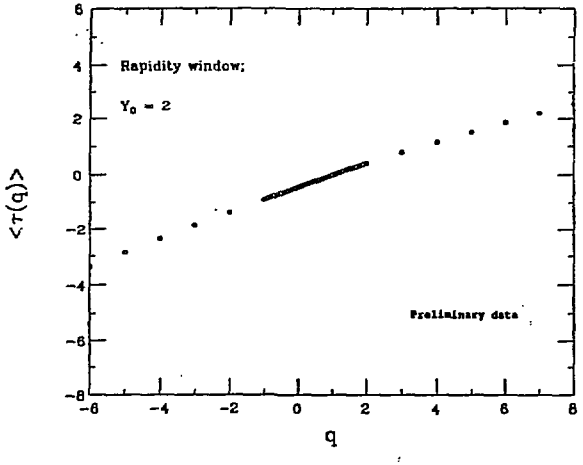

Fig. 39

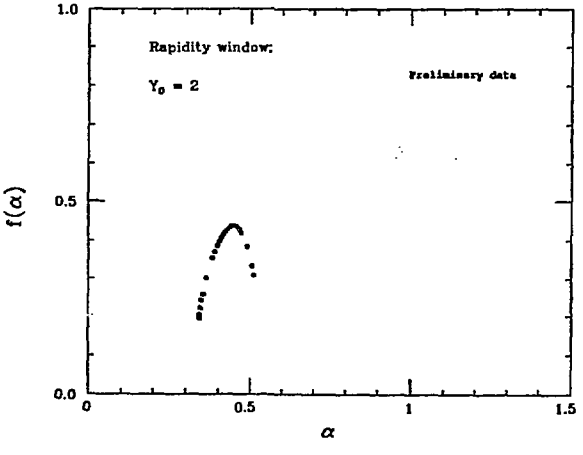

Fig. 40

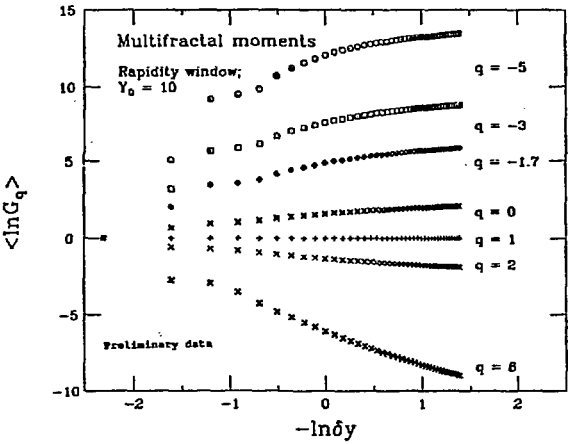

Fig. 41

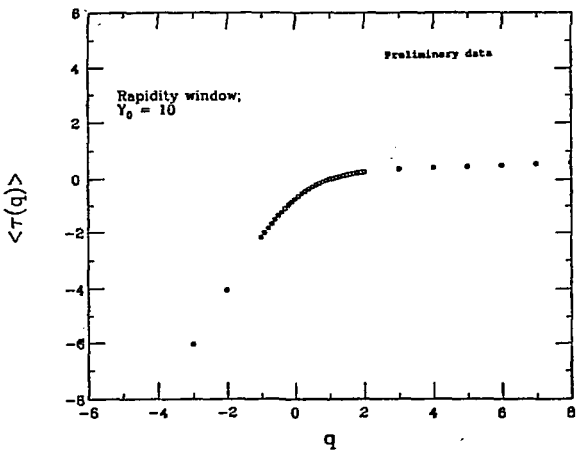

Fig. 42

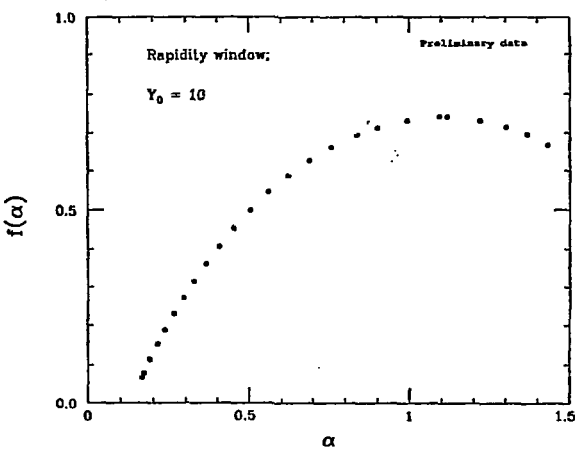

Fig. 43

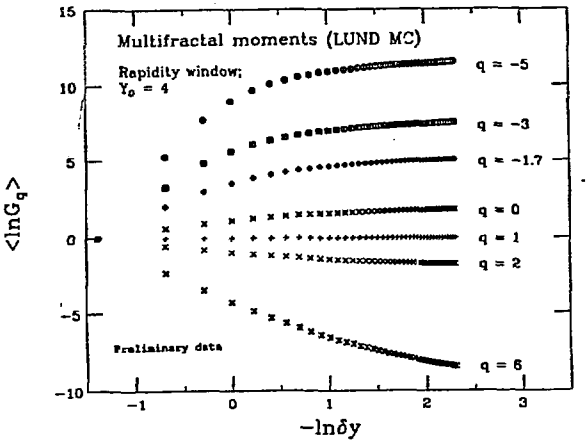

Fig. 44

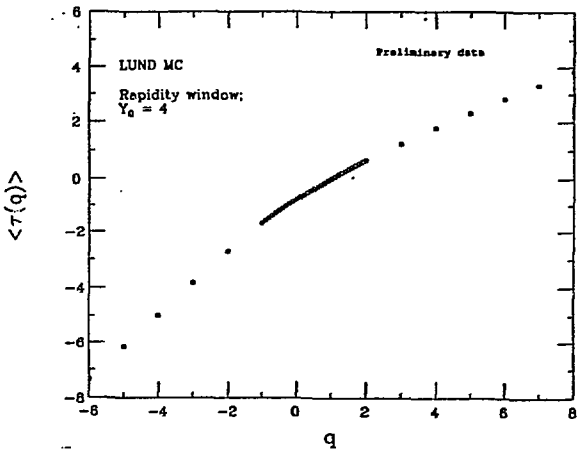

Fig. 45

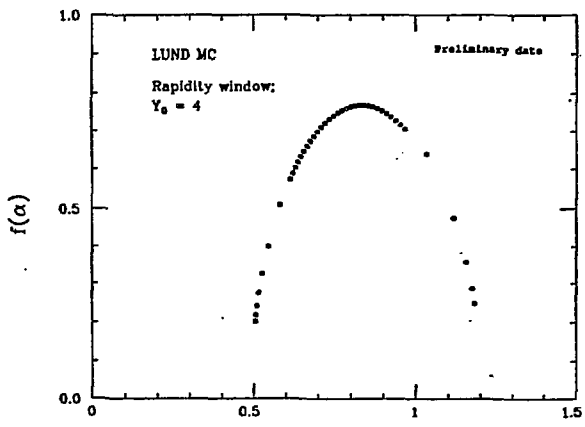

Fig. 46